



Symmetric coalescence of two hydraulic fractures

Niall J. O’Keeffe^{a,1}, Zhong Zheng^{a,b,c}, Herbert E. Huppert^a, and P. F. Linden^a

^aDepartment of Applied Mathematics and Theoretical Physics, University of Cambridge, Cambridge CB3 0WA, United Kingdom; ^bBP Institute, University of Cambridge, Cambridge CB3 0EZ, United Kingdom; and ^cDepartment of Earth Sciences, University of Cambridge, Cambridge CB2 3EQ, United Kingdom

Edited by David A. Weitz, Harvard University, Cambridge, MA, and approved August 27, 2018 (received for review May 30, 2018)

The formation of a fracture network is a key process for many geophysical and industrial practices from energy resource recovery to induced seismic management. We focus on the initial stage of a fracture network formation using experiments on the symmetric coalescence of two equal coplanar, fluid-driven, penny-shaped fractures in a brittle elastic medium. Initially, the fractures propagate independently of each other. The fractures then begin to interact and coalesce, forming a bridge between them. Within an intermediate period after the initial contact, most of the fracture growth is localized along this bridge, perpendicular to the line connecting the injection sources. Using light attenuation and particle image velocimetry to measure both the fracture aperture and velocity field, we characterize the growth of this bridge. We model this behavior using a geometric volume conservation argument dependent on the symmetry of the interaction, with a 2D approximation for the bridge. We also verify experimentally the scaling for the bridge growth and the shape of the thickness profile along the bridge. The influence of elasticity and toughness of the solid, injection rate of the fluid, and initial location of the fractures are captured by our scaling.

hydraulic fracturing | coalescence | hydrogel | self-similarity | fractures

Fluid-driven fracturing involves the propagation of a fracture within a solid due to pressure applied by a fluid. This technique has predominantly been used in unconventional energy reservoirs with low permeabilities that make the resource difficult to extract (1). The creation of fractures increases the overall permeability of the rock formation, providing easier paths for hydrocarbons to escape. Individual fractures within these formation networks can interact with each other by coalescing and altering propagation directions, which will have a large influence of the success of an operation. Other applications that may include similar coalescence dynamics are measurement of existing (in situ) stresses (2), carbon sequestration (3), geothermal energy recovery (4), magma transport (5), compensation grouting (6), and disposal of liquid waste underground.

Recent experimental studies on single penny-shaped fractures successfully captured the dynamic behaviors for the propagation under two different dominant energy dissipation mechanisms: viscous dissipation and material toughness (7–9). In this paper, we focus on the coalescence of two fluid-driven, penny-shaped fractures when the fracture is dominated by the material toughness (rather than viscous dissipation) and provide experimental observations and scaling arguments on the dynamic behavior during the growth of bridges formed between two fractures. While the experiments and model are simplifications of the practical applications, the understanding of the physical mechanisms of fracture coalescence provides insights into the initial stage of fracture network formation and may have implications in some of the applications previously noted.

Experimental Setup

To investigate the coalescence of hydraulic fractures, we designed a dual-fracturing experimental setup, which consists of two injection needles with radii of 0.81 mm set in a polyacrylamide hydrogel of dimensions 100 × 100 × 77 mm (Fig. 1). Four polycarbonate plates of 1 mm were introduced into the sides of the acrylic container to impose a small initial principal stress

perpendicular to the needle, which sets the direction of fracture propagation. The plates ensured that the two tensile fractures coalesced approximately on the same plane as long as the needle positions were fixed to the same depth into the gel. The two needles were placed a distance l_0 apart. This distance l_0 (30–40 mm) was sufficiently large that any rapid fracture due to initiation (radius $\lesssim 5$ mm) around the needle tip did not influence the dynamics of coalescence; l_0 was also chosen to be sufficiently small that the finite size of the container did not affect fracture propagation.

The hydrogels used in the experiments were transparent, enabling detailed optical measurements. They were also brittle and elastic, allowing significant variation in both Young’s modulus E and fracture toughness K (10). Newtonian fluids, water–glycerin mixtures with different dynamic viscosities μ , were injected at constant volumetric rates Q_0 into the hydrogel using a syringe pump (HA PhD Ultra). The experimental parameters (*Materials and Methods*) were chosen so that the fractures propagated in the toughness-dominated regime before coalescence (7, 9, 11).

Mathematical Model and Experimental Results

A representative time evolution of the interaction between the two fractures is shown in Fig. 2. Initially, the two fractures propagated independently of each other as standard penny-shaped fractures in the x - y plane, where the injection needles were aligned along the x axis, and the distance between the fractures gradually reduced (Fig. 2A). When the fractures were sufficiently close, the stress intensity in the hydrogel increased significantly at the inner crack tip nearest to the other fracture (12), which caused the fractures to become attracted to each other. This attraction retards the outer radial growth of each fracture and induces propagation only in the direction of the other cavity, causing coalescence.

Significance

We present an experimental investigation on the coalescence of hydraulic fractures in a brittle solid. Using a dual-fracturing setup, we obtain high-resolution experimental measurements on the time evolution of the fracture profiles and internal velocity field before, during, and after fracture coalescence. These measurements show an intermediate time self-similar coalescence during the dynamic interaction of two fractures. The work probes the dynamic formation of a fracture network, which is crucial to the industrial practice of energy resource recovery, compensation grouting, and the reservoir integrity of many confined systems involving fluid injection.

Author contributions: N.J.O.K., Z.Z., H.E.H., and P.F.L. designed research; N.J.O.K. performed experiments; N.J.O.K. and Z.Z. analyzed data; and N.J.O.K., Z.Z., H.E.H., and P.F.L. wrote the paper.

The authors declare no conflict of interest.

This article is a PNAS Direct Submission.

Published under the PNAS license.

¹To whom correspondence should be addressed. Email: okeeffen@damtp.cam.ac.uk.

This article contains supporting information online at www.pnas.org/lookup/suppl/doi:10.1073/pnas.1809233115/-DCSupplemental.

Published online September 25, 2018.

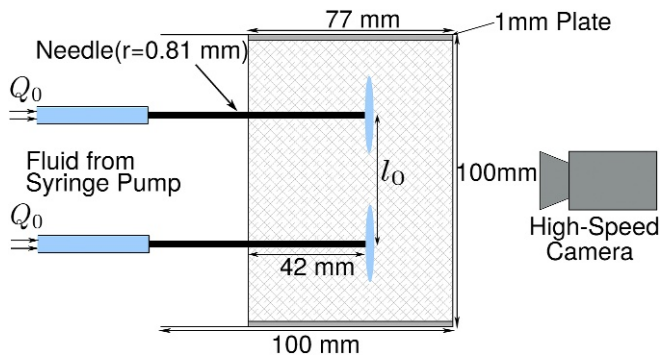


Fig. 1. Schematic of the dual-fracturing experimental apparatus. Fluid is injected from two separate syringes on a dual-syringe pump to ensure an equal injection rate into each fracture, both of which are generated on the same plane.

The fractures were observed to coalesce and form a narrow bridge at a particular time (which we denote by $t = 0$). Shortly after coalescence, we observed that significant fracture growth only occurred in the region close to the bridge, which caused a rapid growth of this bridge (Fig. 2*B*). When the bridge length $2d$ became comparable with the diameter $2R_0$ of each fracture, growth spread to the entire envelope of the two interacting frac-

tures. As time progressed, the two fractures gradually became indistinguishable and approached the shape of a standard single radial fracture in the toughness-dominated regime (with injection rate $2Q_0$). Particle image velocimetry (PIV) measurements are provided for each stage of the fracturing and coalescing process in Fig. 2*A–E*. We can see from Fig. 2*A* that, initially, the flow was mostly radial, similar to that observed for single fractures (7). Then, after the fractures coalesced, the flow everywhere was attracted toward the bridge, and a large increase in velocity occurred in the vicinity of the bridge (Fig. 2*B*). After this initial spike in velocity and as the bridge began to grow, a stagnation point appeared in the center of this bridge, with velocity vectors pointing along the bridge in the y direction toward its edges (Fig. 2*C–E*).

In Fig. 2*F* and *G*, we can see the evolution of coalescence along the x - z plane, where the fracture is assumed to be symmetric about its midplane. Shortly after the fractures first touched, the profile in this plane centered at the point of coalescence can be seen to level out quickly. A 3D image of the bridge at a particular time is also shown in Fig. 3, where the full shape of the bridge and its roughness can be seen.

Mathematical Model. The interface shape in the x - y plane motivates us to explore the behavior for the growth of the bridge shortly after the coalescence of two fractures. In particular, we investigate the growth of the bridge length $2d$ using a

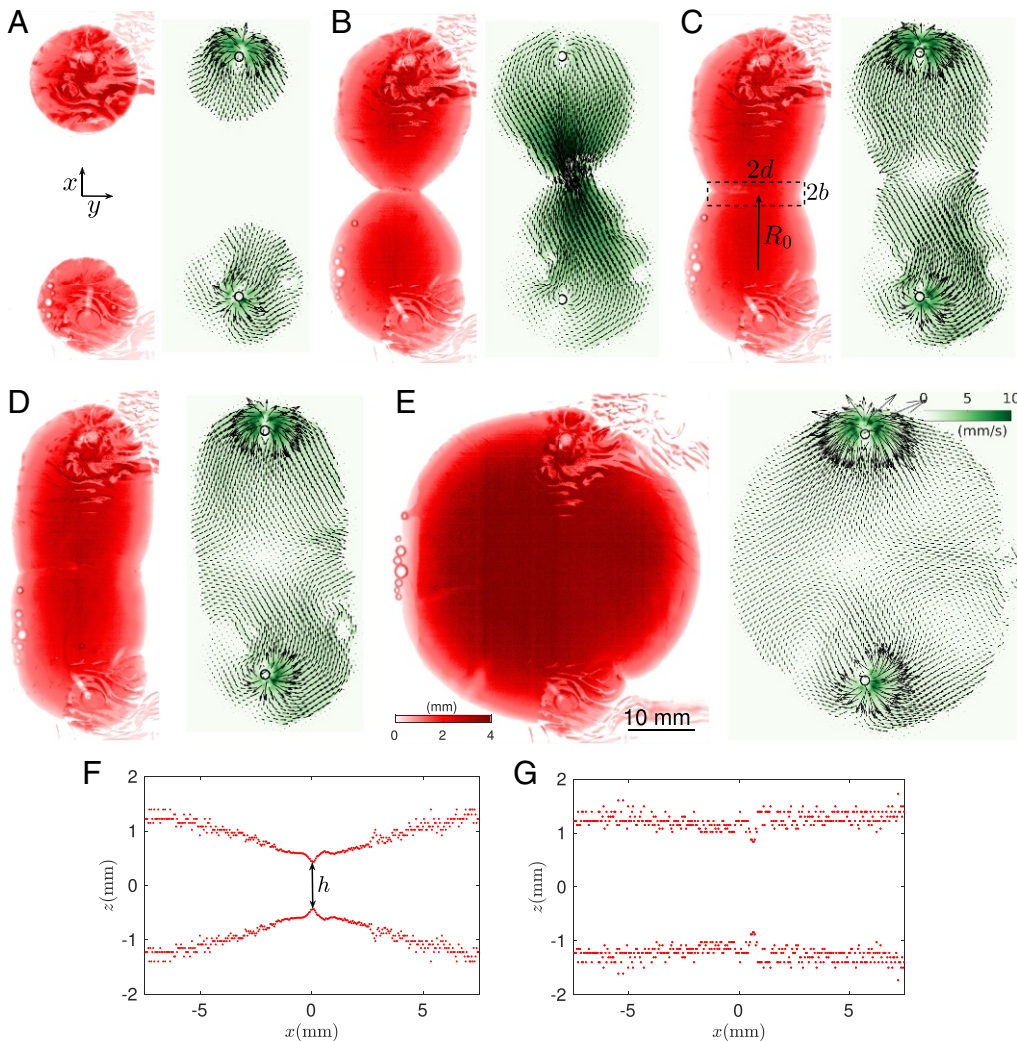


Fig. 2. Time evolution of the coalescence process of two fractures. (A–E) Top view images and (F and G) side view images. The times at which the images were taken are (A) $t = -6$ s, (B) $t = 0.01$ s, (C) $t = 0.8$ s, (D) $t = 2.5$ s, (E) $t = 21$ s, (F) $t = 0.04$ s, and (G) $t = 0.6$ s. The noise in *F* and *G* is an artifact of the calibration. Both light attenuation (experiment 1) and PIV (experiment 6) measurements are used (but not simultaneously for the same experiment), and in *A–E*, we show the fracture thickness and velocity field from two repeated experiments at the same times. The distortion of light in the dyed images is due to the presence of injection tubes connected to the syringe pump. The color bar of the PIV images corresponds to the velocity magnitude, and values shown in *B* are four times those in other top view images.

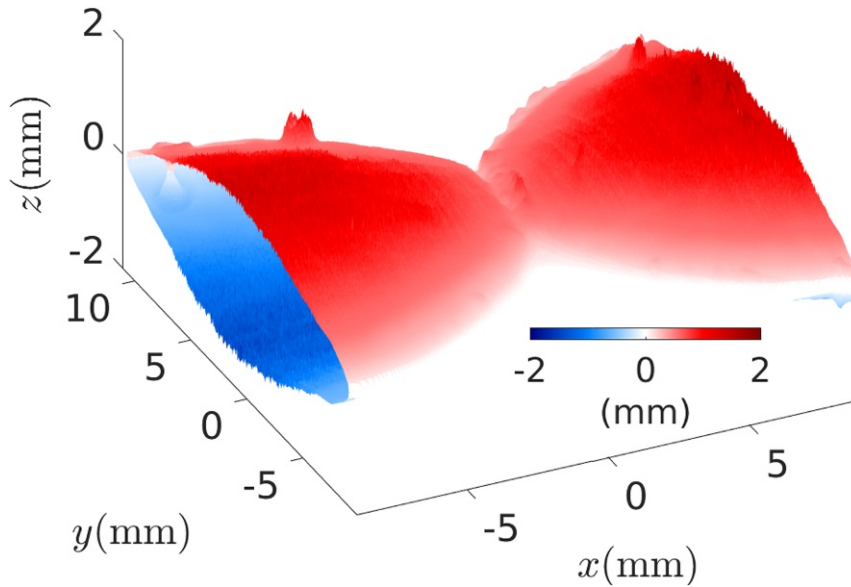


Fig. 3. 3D image of the bridge formed during the coalescence of two fractures in experiment 1 at $t = 0.04$ s.

volume conservation argument surrounding a local region at the point of coalescence (13–17). We consider a box around the bridge of volume V (Fig. 2C) with length $2d$, width $2b$, and height h . Assuming that the individual fractures are circular, geometry implies that $b = R_0 - (R_0^2 - d^2)^{1/2} \approx d^2/2R_0$, provided that $d \gg b$. Thus, the volume of this box is $V \approx 4dbh \approx 2d^3h/R_0$. The PIV experiments further illustrate that, after a very brief initial increase, the flow rate into either side of the box settles to a constant value and is approximately the imposed injection rate Q_0 (Fig. 4). It follows that

$$\frac{dV}{dt} \approx \frac{2d^3h}{R_0t} \approx 2Q_0, \quad [1]$$

which provides the scaling relation for the length of the bridge

$$d \approx \left(\frac{Q_0 R_0}{h} \right)^{1/3} t^{1/3}. \quad [2]$$

Note that the scaling relation [2] is dependent on the height h of the bridge. Consequently, to obtain a relationship for the bridge height evolution with time, we further assume that the bridge section can be approximated as a 2D fracture. The pressure p inside the 2D fracture is $p \approx E'h/d$, where $E' = E/(1 - \nu^2)$ is the plane strain modulus and ν is the Poisson ratio (18). Assuming that the dominant energy dissipation mechanism for the growth of the bridge is through fracture tip opening rather than viscous dissipation, the fracture propagation condition yields $pd^{1/2} \approx K$, where $K = \sqrt{2\gamma_s E'}$ is the material toughness and γ_s is the fracture surface energy of the material (11, 19, 20). Combining this propagation condition, the pressure relation $p \approx E'h/d$, and the mass balance equation [1], we establish the following scaling relations for the bridge length and height:

$$d \approx \left(\frac{Q_0 R_0 E'}{K} \right)^{2/7} t^{2/7} \quad \text{and} \quad h \approx \left(\frac{Q_0 R_0 K^6}{E'^6} \right)^{1/7} t^{1/7}. \quad [3]$$

Eq. 3 incorporates the influence of fluid injection rate Q_0 , the Young's modulus E and material toughness K of the solid, and the distance $2R_0$ between the fracture centers at the moment of coalescence.

Experimental Results. The experimental measurements of the bridge length $2d$ for various parameters are plotted in Fig. 5A. We further rescale the raw data for d based on the bridge scaling equation [3], which leads to a convincing collapse onto a single curve in Fig. 5B. The best power law fit $d = \alpha_1 (Q_0 R_0 E'/K)^{2/7} t^{\beta_1}$ through the rescaled data during times when $d \lesssim R_0$ after coalescence provides a dimensionless prefactor of $\alpha_1 = 0.81 \pm 0.07$ and exponent $\beta_1 = 0.31 \pm 0.02$. Similarly, we can analyze the experimental data for the bridge height growth at the point of coalescence in Fig. 5C. We measure h by using a 10-pixel average around the point of coalescence. Rescaling the data according to equation [3], we again obtain a reasonable collapse (Fig. 5D). The best fit has the form $h = \alpha_2 (Q_0 R_0 K^6/E'^6)^{1/7} t^{\beta_2}$. Fitting this form for early times of bridge growth, we obtain $\alpha_2 = 2.5 \pm 0.2$ and exponent $\beta_2 = 0.14 \pm 0.03$. The data collapse in both d and h , and the agreement of the fitting exponents, within error bounds, with the theoretical values in Eq. 3 indicate that we have successfully captured the initial bridge formation process during the fracture coalescence experiments.

The height profile along the bridge in the y - z direction is shown in Fig. 6A. Using the toughness height scaling equation [3], we collapse the thickness profiles at different times to a single elliptical shape (Fig. 6B), which provides additional

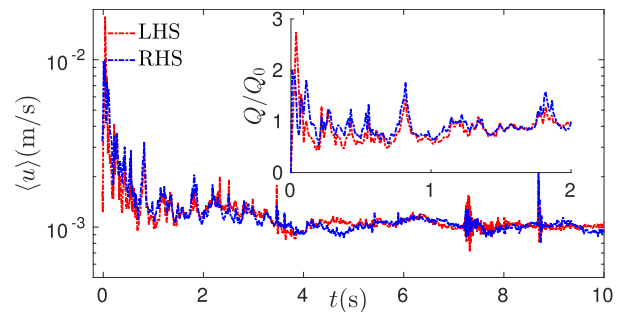


Fig. 4. Measured velocity into the left-hand side (LHS) and right-hand side (RHS) of the bridge box (experiment 6). (Inset) A representative computed volume flux value into each side of the bridge box is constant and approximately Q_0 , the imposed injection rate (SI Appendix).

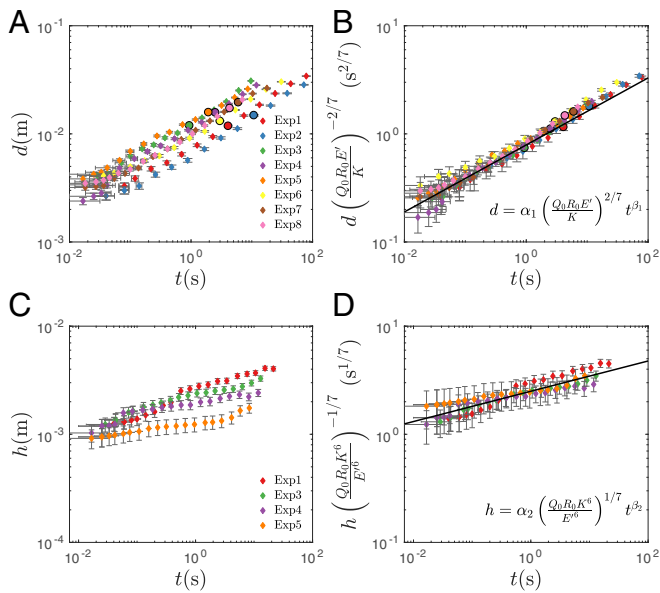


Fig. 5. Experimental measurements of the half bridge length d and height h as a function of time. (A) Raw data of d . (B) Rescaled data of d according to Eq. 3. (C) Raw data of h . (D) Rescaled data of h using Eq. 3. The points where $d \approx R_0$ are denoted by the circular markers in A and B. The data collapse in B and D indicates that the scaling argument [3] captures the fracture coalescence dynamics. In addition, power law fits provide $\alpha_1 = 0.81 \pm 0.07$, $\beta_1 = 0.31 \pm 0.02$, $\alpha_2 = 2.5 \pm 0.24$, and $\beta_2 = 0.14 \pm 0.03$. The scaling exponents are also consistent with Eq. 3.

evidence that the major resistance for bridge growth in our experiments is dominated by fracture tip opening. The time evolution of the profile shape is further examined in this initial stage of coalescence in Fig. 7A, where $d_s(x, t)$ represents the profile shape above the line $y=0$ connecting the injection points and hence, $d(t) = d_s(0, t)$. The shape evolution also suggests a local universal behavior: rescaling the data using the geometric relationship leads to good data collapse around the minimum (Fig. 7B).

We note that the resistance for the bridge growth is dominated by material toughness in these experiments. We anticipate the existence of another regime when the dominant energy dissipation mechanism is viscous drag, which is currently under investigation. We also note that, at very late times, the coalescing hydraulic fractures fully merge and propagate as a single penny-

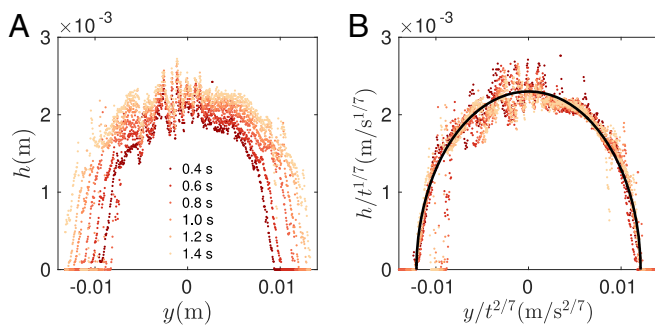


Fig. 6. Experimental measurements of the time evolution of the bridge height profile h in the y - z plane (experiment 3). (A) Raw data; (B) rescaled data using Eq. 3. The rescaled bridge heights collapse to a universal profile, which has an elliptical shape (bold line). The noise in the data is from surface roughness along the bridge. The elliptic fit has semimajor and -minor radii of 1.2×10^{-2} and 2.3×10^{-3} , respectively.

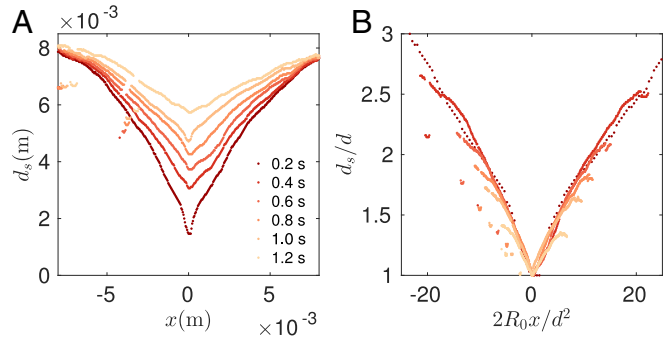


Fig. 7. Experimental measurements of the time evolution of the fracture profile on the x - y plane following the coalescence of two fractures (experiment 1). (A) Raw data; (B) rescaled data. The rescaled profiles, according to $b \approx d^2/2R_0$, collapse to a universal shape near the minimum in B, which suggests a local self-similar dynamic behavior during the coalescence of two fractures.

shaped fracture, with a radius growing according to $\propto t^{2/5}$ in the toughness regime (SI Appendix).

Conclusions

To summarize, we investigated experimentally the coalescence of two coplanar, penny-shaped hydraulic fractures. In particular, we focused on the early stage of coalescence when two fractures touch each other to form a bridge. We identified the dynamics of the bridge formation process, which provides an aspect involved in the formation of a fracture network. Our study addresses a key understudied facet of a wide range of practical applications in the recovery of subsurface energy resources, such as shale gas and geothermal energy, and induced seismic management from fracturing projects. We also note that heterogeneity is common in many of these applications, and this may have a significant effect on some of the dynamics observed, which provides a direction for future investigation.

Materials and Methods

Experimental Parameters. The experimental parameters used in this paper for each experiment are in Table 1. The distance between the injection points l_0 was varied between 30 and 40 mm. The Young's modulus E was changed by approximately a factor of three from 97 to 320 kPa. The viscosity of the injected fluid μ ranged from 0.28 to 1.13 Pa·s, approximately a factor of four. The volumetric injection rate Q_0 also varied by an order of magnitude from 2.0 to 20 mL/min. The upper constraints of the injection rate for a given fluid viscosity were mainly imposed by the strength of the syringe pump. For the case of a single fracture, the transition timescale $t_{mk} = (\mu^5 Q_0^3 E^{13} / K^{18})^{1/2}$ varies between 10^{-6} and 10^{-4} s for these particular experiments, verifying that it is in the toughness regime pre-coalescence.

Experiments 1–5 use light attenuation, and experiments 6–8 use PIV measurements. All measurements are taken using a high-speed camera (Dalsa Falcon 2 4MP) with a spatial resolution of 1 pixel ≈ 0.037 mm and frames

Table 1. Experiments conducted with particular values of physical parameters

Experiment	l_0 (mm)	E (kPa)	μ (Pa·s)	Q_0 (mL/min)	γ_s (Jm $^{-2}$)
Experiment 1	40	97	1.13	5.0	5.2
Experiment 2	40	97	1.13	2.0	5.2
Experiment 3	40	125	1.13	20	4.4
Experiment 4	35	125	0.28	10	4.4
Experiment 5	35	320	0.66	20	3.6
Experiment 6	40	97	0.44	5.0	5.2
Experiment 7	35	157	0.35	5.0	5.2
Experiment 8	30	125	0.37	5.0	4.4

per second ranging between 60 and 120 depending on the experiment. The Digiflow software was used extensively in processing the videos and taking measurements (21). Thickness measurements were obtained from light attenuation experiments that required calibration using a glass wedge of known dimensions. This procedure is detailed extensively in previous studies (9, 10, 22).

Velocity Field. Velocity field information was obtained from PIV experiments. A light sheet of approximately 10 mm was created using two arc lamps and slits on the side of a blacked out chamber holding the hydrogel. The fracturing fluid was then seeded with particles of diameter 40 μm (Orgasol). The particles within the fracture were then illuminated with the light sheet and tracked using a PIV algorithm. The Digiflow software was

used to calculate the corresponding velocity measurements (21). A small amount of fluorescein was also added to the fluid so that the fracture edge could be distinguished but not so much that the light off the particles was saturated. The representative flux Q in Fig. 4 is calculated using $Q \approx \langle u \rangle 2dh$. Since no h measurements are available from PIV experiments, it was estimated using the experimental parameters and the prefactor obtained from the fit in Fig. 5D.

ACKNOWLEDGMENTS. We thank the technicians in the G. K. Batchelor laboratory for their help in setting up the experiment. This work was funded with the support of an Industrial Cooperative Award in Science & Technology (iCASE) from the Engineering and Physical Sciences Research Council (EPSRC) and BP (Grant EP/L505389/1).

1. Economides MJ, Nolte KG (2000) *Reservoir Stimulation* (Wiley, Chichester, United Kingdom), Vol 18.
2. Fairhurst C (1964) Measurement of in-situ rock stresses. With particular reference to hydraulic fracturing. *Rock Mech Eng Geol* 2:129–147.
3. Rudnicki JW (2000) Geomechanics. *Int J Sol Struct* 37:349–358.
4. Murphy HD, Tester JW, Grigsby CO, Potter RM (1981) Energy extraction from fractured geothermal reservoirs in low-permeability crystalline rock. *J Geophys Res Solid Earth* 86:7145–7158.
5. Lister JR, Kerr RC (1991) Fluid-mechanical models of crack propagation and their application to magma transport in dykes. *J Geophys Res Solid Earth* 96:10049–10077.
6. Mair R, Hight D (1994) Compensation grouting. *World Tunnelling Subsurface Excavation* 7:361–367.
7. O’Keeffe NJ, Huppert HE, Linden PF (2018) Experimental exploration of fluid-driven cracks in brittle hydrogels. *J Fluid Mech* 844:435–458.
8. Lai CY, Zheng Z, Dressaire E, Wexler JS, Stone HA (2015) Experimental study on penny-shaped fluid-driven cracks in an elastic matrix. *Proc R Soc A* 471:20150255.
9. Lai CY, Zheng Z, Dressaire E, Stone HA (2016) Fluid-driven cracks in an elastic matrix in the toughness-dominated limit. *Philos Trans R Soc A* 374:20150425.
10. O’Keeffe NJ, Linden PF (2017) Hydrogel as a medium for fluid-driven fracture study. *Exp Mech* 57:1483–1493.
11. Savitski AA, Detournay E (2002) Propagation of a penny-shaped fluid-driven fracture in an impermeable rock: Asymptotic solutions. *Int J Sol Struct* 39:6311–6337.
12. Xiao ZM, Lim MK, Liew KM (1994) Stress intensity factors for two coplanar penny-shaped cracks under uniaxial tension. *Int J Eng Sci* 32:303–311.
13. Paulsen JD, Carmigniani R, Kannan A, Burton JC, Nagel SR (2014) Coalescence of bubbles and drops in an outer fluid. *Nat Commun* 5:3182.
14. Ristenpart WD, McCalla PM, Roy RV, Stone HA (2006) Coalescence of spreading droplets on a wettable substrate. *Phys Rev Lett* 97:064501.
15. Hernández-Sánchez JF, Lubbers LA, Eddi A, Snoeijer JH (2012) Symmetric and asymmetric coalescence of drops on a substrate. *Phys Rev Lett* 109:1–5.
16. Zheng Z, Fontelos MA, Shin S, Stone HA (2018) Universality in the nonlinear leveling of capillary films. *Phys Rev Fluids* 3:032001.
17. Zheng Z, et al. (2018) Healing capillary films. *J Fluid Mech* 838:404–434.
18. Spence DA, Sharp P (1985) Self-similar solutions for elastohydrodynamic cavity flow. *Proc R Soc A* 400:289–313.
19. Kanninen MF, Popelar CL (1985) *Advanced Fracture Mechanics* (Oxford Univ Press, Oxford).
20. Rice JR (1968) Mathematical analysis in the mechanics of fracture. *Fracture: An Advanced Treatise*, ed Liebowitz H (Academic Press, NY), Vol 2, pp 191–311.
21. Dalziel SB (2017) *Digiflow User Guide* (DL Research Partners, Cambridge, UK). Available at www.damtp.cam.ac.uk/lab/digiflow/. Accessed September 20, 2018.
22. Bunger AP (2006) A photometry method for measuring the opening of fluid-filled fractures. *Meas Sci Technol* 17:3237–3244.